ACS OMEGA

http://pubs.acs.org/journal/acsodf

Article

Predictive Model for Concentration Distribution of Explosive Dispersal

Xing Chen, Zhongqi Wang,* En Yang, and Jianping Li

Cite This: *ACS Omega* 2021, 6, 2085−2099

Read Online

ACCESS | Metrics & More | Article Recommendations

ABSTRACT: At present, concentration of explosive dispersal is very difficult and uncertain to measure. Numerical experimentation can avoid this deficiency. Data of particles during dispersal are readily available, including velocity, displacement, and mass. However, there is minimal research on the concentration of explosive dispersal. Existing models used for the calculation of particle concentration neglect measuring the initial condition of particles and cannot, therefore, accurately describe the whole particle dispersion process. Moreover, existing concentration models do not take into account the continuous decrease in the size of particles caused by stripping and evaporation effects during flight, resulting in inaccurate descriptions of the concentration distribution. Consequently, this work derives a model to predict the concentration distribution of liquid and granular material dispersal, considering the two questions above. Concentration can be calculated based on the condensed-phase distribution and gas-phase distribution of the fuel cloud at different times by the model. This model was validated using experimental data on the mean concentration of dispersal and was well fitted. Therefore, it can be used as a tool to predict the dispersal of liquid and granular material, an explosion suppressant in coal mine accidents, and an aerosol fire extinguishant in remote forest fire extinguishers. Moreover, being able to predict the concentration of large-scale dispersal can significantly improve the accuracy and efficiency of secondary detonation.

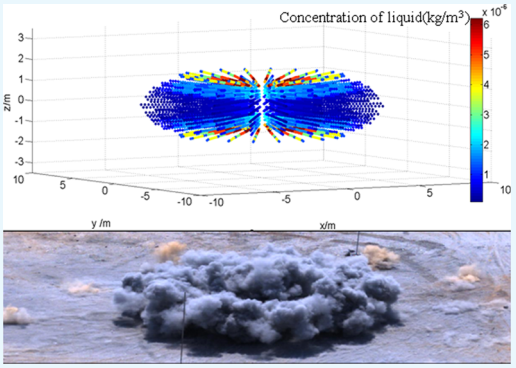

1. INTRODUCTION

Heterogeneous blasts with jet formation have generated widespread interest recently. At present, concentration distribution has become difficult and a hot spot of discussion. A new model for concentration distribution of explosive dispersal is proposed. After detonation of the center charge, the fuel breaks into particles or droplets are distributed at a certain size. Then, the particles or droplets move in air. Due to the effect of air resistance and temperature difference, the particles gradually reduce in size and vaporize during flight. Therefore, a cloud in which the condensed phase coexists with the gas phase is eventually formed. The mechanism of rupture of the shell and the dispersal material, the formation of jet, the number of jets formed, and the size of particles are very important in the study of the concentration of the cloud formed by explosion.

The fragmentation of powders in spherical geometry was discussed by Milne,[1,2] and an analysis of the early phase was conducted. It was proposed that primary fragmentation occurred at a very early stage, which was associated with the time that the release wave from the outer surface reaches the inner surface of the fill. The initial velocity of dispersed particles is influenced by the process of shell fragmentation. Grady[3,4] showed that the surface or interface area created in the fragmentation process was governed by an equilibrium balance of the surface or interface energy and a local inertial or kinetic energy. The macroscopic flow and bulk material properties were explored to determine the particle or fragment size distribution during explosive dissemination. It was found that the number of fragments has little relation to the original particle size, and the observed size of the fragments is related to a large surface energy.

However, in an experiment that focused on the cylindrical explosive dispersal of both bulk liquid and granular solids by Ripley,[5] it was indicated that the initial number of particle jets is associated with the initial particle expansion velocity. According to a dispersal experiment conducted by Frost,[6] liquid produces a larger number of jets than solid particles of the same volume. Furthermore, a dispersal experiment on a solid particle layer saturated with liquid was found to produce almost an order of magnitude more jets than solid or liquid particles alone with a cylindrical geometry device. However, it

Received: October 21, 2020
Accepted: December 30, 2020
Published: January 14, 2021

is not yet possible to predict jet formation effects using current multiphase models. A physical mechanism for the dual-jet structure was proposed by Zhang.[7] The primary jet structures arise from the interior boundary between the charge and the dispersed material. Fine jet instabilities are formed at the outside boundary between the dispersed material and air. The number of primary jets is controlled by the number of inner casing fragments at the explosive payload interface. It is also influenced by the mass ratio of payload to explosive and the inner casing fragment pattern.

In an experiment by Allen[8] examining the mitigation of effects from a blast and the fragmentation of explosives, a potential mechanism was identified that suggested energy is transferred from the blast wave to the disseminated particles or droplets by drag. Therefore, the size of particles and jet formation appear to play a role in the efficiency of this mechanism. According to Wang,[9] it was proved using the Gurney model that as the ratio of charge mass to fuel mass decreased, more explosion energy was converted into kinetic energy of particles. The velocity distribution of the fragments of the cylinder charge was simulated by Grisaro using the smoothed particle hydrodynamics (SPH) method. It was concluded that the velocity distribution of fragments along the axis was nonuniform.[10] Zhang et al.[11] established a mathematical model for the near-area dispersion of the fuel air explosive under the action of uncoupled charge explosion. The maximum scattering velocity was calculated, and the results were consistent with the experiment. Ding et al.[12,13] carried out a numerical simulation on the explosion suppression device based on the principle of explosive dispersal. Computational fluid mechanics software ANSYS-Fluent was used to simplify modeling the process of water dispersal, cloud formation, and diffusion. The models for near field and far field were built and coupled. The MacCormack scheme is used to solve the whole process of explosive dispersion. This model describes the overall movement of cloud after explosion. However, it is particularly complicated and takes a long time to calculate.

At present, the methods of measuring concentration distribution of explosive dispersal on site are generally expensive, unstable, and inaccurate. A measurement of particle density during explosive particle dispersal based on laser light attenuation was developed to determine the temporal history of particle number density during the explosive dispersal of inert particles by Goroshin.[14] The test results have good correlation with the prediction of qualitative theory in close proximity to the charge. However, the application time of the gauge must be before the time that the soot produced by explosive charge arrives at the testing location.

However, there has been minimal research on the concentration distribution of dispersed fuel. It is very laborious and subjects lots of uncertainty to obtain cloud concentration by measuring tools. Numerical experimentation can avoid this deficiency because particle information is available. However, for existing models on particle dispersion concentration, it is unable to carry out a complete process of numerical simulation for the initial shell breaking, fuel breaking, the subsequent droplet breakage, and cloud dispersion during flight. It means that the particle dispersion process cannot be completely and accurately described. Meanwhile, the reduction in particle size during flight is not taken into account, which affects concentration distribution at each moment. The commercial softwares are more complex and take a long time for calculation.

Therefore, a new particle dispersion concentration model is established in this paper. After taking into account the whole process of explosive dispersal including initial shell rupture, fuel breaking, and droplet stripping during dispersion, mesh dispersion and sample method are used to obtain the concentration distribution of dispersed particles. The calculation speed is very fast, i.e., a few minutes. It will be helpful in designing experiments, selecting experimental objects, and grasping the overall rules before the tests. The fuel velocity and radius are taken as the initial conditions of the particle dispersion model when fuel expands to the point of fracture under the drive of center charge. Evaporation effects caused by temperature differences and stripping effects caused by the particles moving too fast in the air are adopted.

The model of concentration distribution is based on the mechanism of the model for the whole explosive dispersal process proposed in the former research.[13] The model for the whole explosive dispersal process was the combination and simplification of the near-field and far-field processes and can predict the variation of cloud movement during the explosive dispersal process.

In the new model of concentration distribution in this paper, the initial conditions of particle dispersion, including initial velocity and initial particle size, as well as initial radius of cloud, were increased and refined; the initial parameter of explosion field given by instantaneous detonation model was supplemented; the radial and axial motion models of particle dispersion were established; and the empirical setting of flight angle is added to estimate the change of cloud height, which makes the dispersal cloud calculated by the model more consistent with the actual test. The appropriate representative particle motion trajectories can be calculated using the model of the whole explosive dispersal process. Therefore, the concentration distribution of particles during dispersal can be obtained by discretizing the particles or droplets dispersal motion trajectories on a rectangular Cartesian mesh and accounting for local sources of mass loss (stripping and evaporation). In the new model, the sample method, weighted average algorithm, and surface fitting and correction were adopted to achieve concentration distribution.

2. MODELING AND ANALYZING THE CONCENTRATION DISTRIBUTION OF DISPERSED FUEL

2.1. Concentration Distribution Model. A single-center tube-type cylindrical dispersal structure as the basic dispersal structure is modeled here. The cylinder shell is filled with liquid fuel or solid−liquid mixed fuel, and there is a center charge in it. In the formation stage of cloud dispersal, no diffusion is considered. Therefore, cloud concentration consisted of condensed-phase concentration formed by the liquid and granular materials and gas concentration formed by the evaporation of droplets.

The concentration of the condensed phase formed by the liquid and granular materials is the main part of the whole concentration of the cloud that is in the heterogeneous mixed state.[16]

2.1.1. Initial Particle Conditions. A single-center tube-type cylindrical dispersal structure with finite length is modeled. The cross section of the cylindrical dispersal structure is shown in Figure 1.

https://dx.doi.org/10.1021/acsomega.0c05128
ACS Omega 2021, 6, 2085−2099

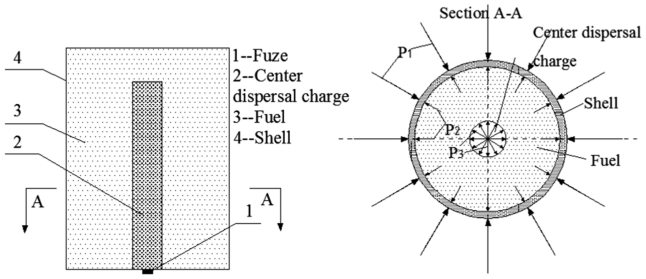

Figure 1. Stress state of the fuel ring. (P_1 is the air pressure on the outer surface of the shell; P_2 is the constraining force of the shell; P_3 is the driving pressure of the detonation product of the center dispersal charge.).

The process of the whole explosive dispersal is as follows: the central charge detonates; shell breaks; the fuel (liquid or granular-liquid material) expands and breaks to form large particles or droplets; particles or droplets move in air while evaporation and stripping decrease the particle or droplet size; and a gas−liquid or gas−granular-liquid multiphase cloud is formed.

2.1.1.1. Instantaneous Detonation Model. The initial parameters of explosion field are given by the instantaneous detonation model. It can be described as follows: the influence of detonating position of explosive is ignored. After detonation, the detonation wave propagates within the charge. Under the action of rigid wall, the detonation wave is reflected many times, reaching the average state that all parameters are equal everywhere. The particle velocity is zero, and the density is the initial explosive density. Taking the equation of state as the polytropic equation, the instantaneous detonation pressure P_m (P_2) is given by the following equation

$$P_m = \frac{\rho_0 C^2}{k} \tag{1}$$

where m is the order of coincidence time, c is the speed of sound, and k is the polytropic exponent. The averaging process of detonation product parameters is analyzed using one-dimensional unsteady fluid mechanics theory and entropy condition. After infinite reflection of shock wave and sparse wave, the average instantaneous detonation sonic velocity C is obtained as half of the detonation velocity D.[17]

$$\lim_{n\to\infty} C = \frac{D}{2} \tag{2}$$

where n is the number of reflections of shock waves on the wall. For the coincidence point of the wave, after infinite reflection, the velocity of the shock wave decreases to $D/2$. According to the limit analysis of the preceding flow fields, that is the sound speed c, the instantaneous detonation P_m can be obtained as equal to the CJ detonation pressure P_{cj} divided by the polytropic exponent K as follows

$$P_m = \frac{\rho_0 D^2}{4k} = \frac{P_{cj}}{k} = \frac{\rho_0 D^2}{12} \quad (k = 3) \tag{3}$$

2.1.1.2. Dispersive Charge Detonation Products Expansion Model.

$$\frac{p}{p_0}\left(\frac{v_0}{v}\right)^{\gamma} = \left(\frac{a_0}{a}\right)^{2\gamma} \tag{4}$$

where v_0 and p_0 are, respectively, the volume and pressure of the detonation products of the instantaneous detonation; v is the volume of detonation products in the process of expansion; p is the pressure of detonation products in the process of expansion; γ is the index of detonation products; and a_0 is the radius of the center tube before expansion.

2.1.1.3. Rupture Model of Shell and Fuel. Taylor et al.[18] studied the broken cylindrical shell by high-speed photographic records and concluded that an axial crack first appeared in the outer wall. Then, the crack gradually widened with the expansion of the shell. Until the diameter of the pipe expanded doubled, the crack penetrated the inner wall, causing the shell to break. Therefore, the shell breaks in the condition that the compressive stress zone of σ_θ disappears and the crack penetrates the inner wall.

The process of shell and fuel ring rupture is simplified for fast analysis and calculation. The motion of shell is in one-dimensional radial. The stress wave is reflected many times during expansion of the shell. Therefore, the propagation of stress waves is not considered in this model. The rigid plastic material model is adopted without considering the elastic stage due to the large deformation of the shell.

The motion process of the shell can be tracked by eq 5[15]

$$w_b = \frac{p_2 - p_1 - 1.15\sigma_Y^D \ln\frac{c}{b}}{\rho b \ln\frac{c}{b}} - \frac{u_b^2}{b}\left(1 - \frac{1 - \frac{b^2}{c^2}}{2\ln\frac{c}{b}}\right) \tag{5}$$

where w_b represents the acceleration of the inner wall of the shell, which is equal to the acceleration of the outer wall of the fuel in the expansion phase; P_1 is the pressure on the outer wall of the shell caused by the air; P_2 is the pressure at the inner wall of the shell passed by the fuel; b and c represent the inner radius and outer radius of the shell in the deformation process, respectively; u_b and u_c represent the particle velocities of the inner wall and outer wall of the shell, respectively, which are equal to the velocity of the outer wall of the fuel in the expansion phase; u_c represent the particle velocity of the outer wall of the shell; and σ_Y^D is the dynamic yield stress for the material.

Before the shell breaks, the fuel (dispersal material layer) expands under the driving force of charge. At the same time, it is constrained by the shell. After the shell breaks, the fuel is affected by the driving force of the explosive product of the charge and the external air resistance. Because the shell fragments have less effect on the dispersal of the particles, the factors are complex. It is assumed that the impact of the shell debris on the fuel is ignored. Then, the fuel breaks into fuel fragments. It is supposed that the fuel fragment is spherical and the characteristic scale of the fuel fragment is an average radius.

In the destruction process of the fuel, the fuel compressed by shock waves is considered an incompressible medium. The fuel breaks under the condition that the compressive stress zone of σ_θ disappears and the crack penetrates the inner wall.

$$w_a = \frac{p_3 - p_2 - 1.15\sigma_{Yf}^D \ln\frac{b}{a}}{\rho a \ln\frac{b}{a}} - \frac{u_a^2}{a}\left(1 - \frac{1 - \frac{a^2}{b}}{2\ln\frac{b}{a}}\right) \tag{6}$$

https://dx.doi.org/10.1021/acsomega.0c05128
ACS Omega 2021, 6, 2085−2099

$$\begin{cases} u_a = w_a \cdot \Delta t \\ u_b = w_b \cdot \Delta t \\ u_0 = \dfrac{1}{2}(u_a + u_b) \end{cases} \tag{7}$$

In eq 6,[15] w_a represents the acceleration of the inner wall of the fuel, w_b represents the acceleration of the outer wall of the fuel, P_2 represents the pressure on the outer wall of the fuel generated by the air, P_3 represents the pressure on the inner wall of the fuel ring generated by the central charge explosion, a represents the inner radius of the fuel ring, b represents the outer radius of the fuel ring, u_a represents the velocity of the inner wall of the fuel ring, u_b represents the velocity of the outer wall of the fuel ring, Δt is the time, and u_0 represents the initial velocity of the fuel.

The initial speed of the particles can be calculated by eq 7. In this model, the average value of the inner fuel ring speed and outer fuel ring speed after expansion before it broke was taken as the initial speed of the fuel fragments u_0 as an approximation.

2.1.1.4. Modification of the Axial Expansion Effect. The dispersal center charge is a finite length cylinder. When the charge is detonated in different ways, the detonation process is affected by the rarefaction wave of an axis. Meanwhile, the impulse acting on the fuel ring varies with the distance from the detonation point. The different impulse caused the changing of the initial velocities of the fuel particles or droplets. The impulse of the detonation product acting on the side wall of a certain section is the integral over time of the pressure acting on the section.

The midpoint of the cylindrical charge serves as the origin of coordinates. The parameter a is introduced: $a = x/l$. L is half the length of the cylindrical charge; x is the distance from a point on the fuel ring to the initiation point along axis. According to eqs 8 and 9 suggested by Zhang et al.,[19] the impulse at the section can be calculated. The detonation methods of charge include end detonation, midpoint detonation, etc. The following calculation in this paper adopts midpoint detonation.

when $0 \le a \le 3/4$;

$$i_a = \frac{i_0}{16}\left[\frac{16 + 23a - 8a^2 - 15a^3}{(1+a)^2} + 3a \ln 2 + 3(1-a)\ln\frac{1+a}{1-a}\right] \tag{8}$$

when $3/4 \le a \le 1$;

$$i_a = \frac{i_0}{32}\left[-5 + 59a - 48a^2 + \frac{1 + 9a + 3a^2 - 5a^3}{(1+a)^2} + 6a \ln\frac{3-2a}{a} + 6(1-a)\ln\frac{2(1+a)}{2a-1} + 24a(1-a)(2a-1)\ln\frac{(2a-1)(3-2a)}{4a(1-a)}\right] \tag{9}$$

where i_0 is the largest impulse applied on the inside wall of fuel ring and i_x is the impulse of the inside wall of the fuel ring at point x. Then, the specific impulse calculated by eqs 8 and 9 is shown in Figure 2.

$$\begin{cases} u_x' = u_0 \cdot \cos\partial \cdot i_a \\ u_y' = u_0 \cdot \sin\partial - u_f \end{cases} \tag{10}$$

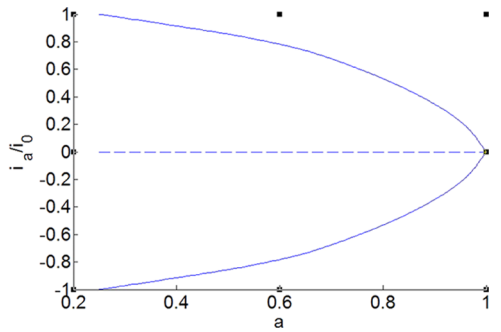

Figure 2. Specific impulse on the side wall of a column charge at midpoint detonation.

where u_x' and u_y', respectively, represent the initial velocity in the radial and axial direction, u_f represents the falling speed of the dynamic dispersal device, i_a represents the impulse on the side wall of a column charge at midpoint detonation, and ∂ represents a dispersion angle. It helps us to obtain the vertical displacement of the dispersed particles or droplets. It can be obtained by eqs 11 and 12.

$$A = ar\tan(k \cdot c \cdot \Delta t) \tag{11}$$

$$\partial = -A + (2 \cdot i - 1) \cdot A/N \quad (i = 1, 2, 3, \ldots, N) \tag{12}$$

In eq 11, k is the empirical coefficient and c is the sound speed. The cylindrical dispersal device is uniformly divided into N segments along the axis that is N fuel rings. When the fuel ring expands and breaks, the angle between the velocity direction and the axis of the fuel block is the angle of flight. The dispersion angle of fuel blocks varies with the axial position of the fuel blocks. The dispersion angle of fuel blocks at both ends of the cylindrical dispersal device is the largest, and the dispersion angle near the axis midpoint becomes smaller. The dispersion angle of fuel block at the center of the cylindrical dispersal device axis is 0.

2.1.2. Particle or Droplet Crushing Model. The droplets decrease in size due to the evaporation effect and stripping effect during moving forward. Furthermore, aerodynamic friction exists on the droplet surface due to the velocity difference between the liquid and gas phases, so the little drops caused by the stripping effect are converted into the gas phase. This can explain in another way why the numbers of fragments at early and late times are very similar according to Milne's research.[1]

The evaporation of droplets is caused by temperature differences and heat exchange between the air and fuel. The Eidelman evaporation model is adopted.[17] It is assumed that the whole surface of the droplet evaporates evenly. The temperature of the droplets is constant in the evaporation process.

$$\frac{dl}{dt} = -\frac{3k_{GAS}N_u(T - T_L)}{\pi l \rho_L^{ini} L} \tag{13}$$

where ρ_l^{ini} represents the density of fuel particle or droplet, k_{GAS} represents the heat conductivity of air, N_u represents the Nusselt number, T/T_L is the temperature of the air/

https://dx.doi.org/10.1021/acsomega.0c05128
ACS Omega 2021, 6, 2085−2099

temperature of the droplets (K), and $(T - T_L)$ is a constant. In the model, it is assumed that the whole surface of the droplet evaporates evenly and the temperature of the droplet remains constant during evaporation. Particle temperature, air temperature, and sound velocity are taken as constants, among which the particle temperature and air temperature vary according to experimental conditions and site seasons. Here, a temperature difference of 20° is adopted. L is the heat of evaporation of droplets (J/kg).

The stripping effect of the fuel particles or droplets is mainly resulted from friction, which is caused by the relative motion of air and fuel particles or droplets. According to Engel,[21] the stripping rate can be described by eq 14. The surface of the droplet starts to peel off due to their very fast movement in air.

$$\frac{\mathrm{d}l}{\mathrm{d}t} = -\left(\frac{\rho\mu}{\rho_L^{\mathrm{ini}}\mu_L}\right)^{1/6}\left(\frac{\mu_L}{\rho_L^{\mathrm{ini}}}\right)^{1/2}|u - u_L|^{1/2} l^{-1/2} \tag{14}$$

where ρ represents the density of the air, μ and μ_L are the viscosity coefficients of the air and fuel, respectively, u represents the speed of the air, u_L represents the speed of fuel, and l represents the average size of the particles or droplets.

The size of the transformed particles or droplets is the sum of the stripping effect and evaporation effect according to the research by Eidelman,[20] and δ is the variation in droplet size in eq 15.

$$\delta = \frac{9k_{GAS}N_u(T - T_L)}{\pi l^2 \rho_L^{\mathrm{ini}} L} + 3\left(\frac{\rho\mu}{\rho_L^{\mathrm{ini}}\mu_L}\right)^{1/6}\left(\frac{\mu_L}{\rho_L^{\mathrm{ini}}}\right)^{1/2} |u - u_L|^{1/2} l^{-3/2} \tag{15}$$

Particle temperature, air temperature, and sound velocity are taken as constants, among which particle temperature and air temperature vary according to the experimental conditions and the site seasons. A temperature difference of 20° is adopted in the following model calculations. The sound speed is 340 m/s at 20 °C.

$$\begin{cases} a = a_1 + u_a \cdot \Delta t \\ b = \sqrt{b_1^2 - a_1^2 - a^2} \\ d_1 = b - a \\ d = d_1 + \delta \cdot \Delta t \end{cases} \tag{16}$$

where the initial particle diameter d_1 is calculated using the initial inner radius of the fuel ring a_1, the initial outer radius of the fuel ring b_1, the particle's initial diameter d_1, and the particle's diameter varying with time d. Milne[1] proposed that the width of the initial fragments is related to the thickness of the compacted layer. In this model, as an approximation, the thickness of the fuel before it broke was taken as the maximum size of the initial fuel fragments.

A simple crushing function is adopted to the initial fuel particles to grade the size.

$$d_i = d_1 \cdot i \cdot \frac{1}{m+1} \quad (i = 1, 2, 3, \cdots, m) \tag{17}$$

where (d_i, d_{i+1}) is the distribution interval of particle size, m is the number of distribution intervals of the particle size, n is the total number of the particles, and $\frac{n}{m-1}$ is the number of particles distributed in the same particle size range. Here, it is assumed that the number of distributed particles within each particle size range remains the same.

2.1.3. Particle or Droplet Motion Model. 2.1.3.1. Single-Particle Motion Dynamics Model and Modification of Particle Group Resistance Coefficient. To simplify the model and calculate quickly, the particles or droplets can be modeled by single-particle motion dynamics in which the collisions between fuel particles or droplets are ignored. The particles are primarily affected by the force drag and gravity. Thus, the other forces are ignored here. The calculation formula of the particle Reynolds number is shown in eq 18

$$Re = \frac{d_p \rho_f}{\mu}|u_f - u_p| \tag{18}$$

where u_f and ρ_f represent the velocity and density of the fluid, respectively, and u_p represents the speed of the particles.

Moreover, because of the interaction between particles, the particle group resistance coefficient was added. According to Schiller et al.[22] and Wen et al.,[23] the drag coefficient of the particle group can be concluded as eq 19.

$$C_D = \begin{cases} \frac{24}{Re}(1 + 0.15Re^{0.687})\cdot\alpha^{-4.7}, & Re < 1000 \\ 0.44, & Re \geq 1000 \end{cases} \tag{19}$$

where C_D represents the drag coefficient and α represents the void fraction.

Therefore, the initial position and initial velocity of the particle or droplet can be obtained.

$$\begin{cases} \omega_f = \frac{\rho \cdot S}{2m} \cdot u_x^2 \cdot C_D \\ R_x' = 0.5(b + a) \\ u_x = u_x' + \omega_f \cdot \Delta t \\ R_x = R_x' + u_x \cdot \Delta t \end{cases} \tag{20}$$

$$\begin{cases} \omega_f' = \frac{\rho \cdot S}{2m} \cdot u_y^2 \cdot C_D \\ R_y' = \frac{h}{2} + (R_x' - b_1)\cdot\tan\partial \\ u_y = u_y' + \omega_f' \cdot \Delta t \\ R_y = R_y' + u_y \cdot \Delta t \end{cases} \tag{21}$$

where S represents the windward area of the particles: $S = \pi r_p^2$, and m represents the mass of the particle or droplet: $m = 4/3\pi(d/2)^3\rho_L^{\mathrm{ini}}$, where the particle diameter d can be calculated as shown in eq 16.

Therefore, combined with the above, the motions of particle or droplet can be described as eqs 20 and 21, respectively, where ω_f represents the deceleration caused by the resistance of the particles due to their movement in the radial direction in the air and ω_f' represents the deceleration caused by the resistance of the particles in the axial direction in the air. The flight angle ∂ is added by empirical setting to estimate the variation of the height of the dispersal cloud. It makes the results calculated by the model more consistent with the experiments. C_D represents the drag coefficient. The average value of the inner radius and outer radius of the fuel ring after

https://dx.doi.org/10.1021/acsomega.0c05128
ACS Omega 2021, 6, 2085−2099

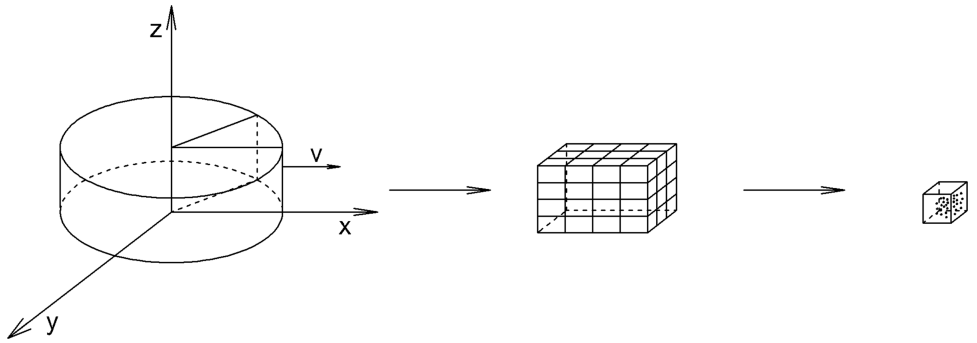

Figure 3. Interception of a small part along the radial from the cylindrical cloud, approximately as a cuboid v; the cuboid is divided into small rectangular boxes of equal volume with a certain size ΔV, and so are the particles or droplets.

expansion is taken as the initial radius of the cloud R'_x, which is the initial position of the particle or droplet in the radial direction; R'_y is the initial position of the particle or droplet in the axial direction; u_x and u_y, respectively, represent the velocity of particle or droplet in the radial and axial directions varying with time; R_x represents the changing radius of the cloud with time in the radial direction, that is, the maximum radial flight distance the particle travels during dispersal; R_y represents the changing radius of the cloud with time in the axial direction, that is, the maximum distance the particle travels during dispersal in the axial direction; and h is the height of the cylindrical dispersal structure.

2.2. Particle Concentration Distribution. *2.2.1. A Cartesian rectangular grid was used to discretize the particle distribution.* Rhodes[24] examined the usefulness of a discrete element method simulation in studying solids mixing in gas-fluidized beds by scanning the bed using a sampling box. The samples method was used to obtain the variance of mixture composition describing the degree of mixing of the particles. Feng[25] studied the mixing and segregation of binary mixtures of particles in a gas-fluidized bed using discrete particle simulation. A fixed sample size was applied, and the contribution to the variance is weighted according to the equivalent number of particles. It is proposed that an appropriate sampling size should be able to properly describe the two extremes: well mixed and fully segregated.

The particles or droplets move in the air after dispersal. The spatial position of the particles changing with time determines the concentration distribution at different times. The particle size and spatial location of the particles or droplets can be calculated by eqs 16, 20, and 21. In this paper, the method is used by dividing the whole approximately cylindrical cloud into small parts on rectangular Cartesian mesh and calculating the concentrations in each part. A small rectangular box is shown in Figure 3. The particles were counted based on their center positions.

The particle cloud formed by dispersal closely resembles a flat cylinder. The method involves dividing the data scatters (the particles or droplets) into small cubes of equal volume with a certain size ΔV, which represents the volume of the small rectangular box. Here, Δx represents the length of the rectangular box, Δy represents the height of the rectangular box, and Δl represents the width of the rectangular box and is a unit of distance. A different number of particles or droplets then fall into each rectangular box. The ratio of the total mass of these particles or droplets to the volume of the small rectangular box is the concentration of the rectangular box (i,j,k) at time t. According to the basic assumption of the discrete element method, since the time step interval is sufficiently small, the velocity and acceleration of the element are constant within a time step.

First, the three-dimensional (3D) matrix grid $(m + 1) \times (n + 1) \times (l + 1)$ is established on the distribution area of the cloud, and the concentration 3D matrix $(m \times n \times l)$ is composed of the concentration of each small rectangular box caused by the grid shown as Figure 4. The distribution area of the grid is

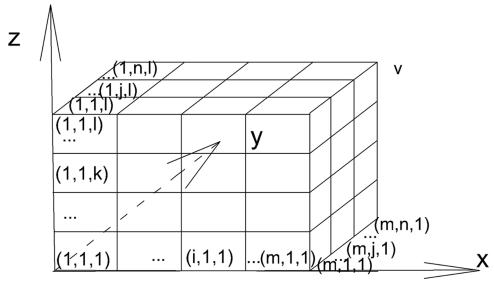

Figure 4. Three-dimensional matrix of concentration distribution $(m \times n \times l)$ for cuboid V.

assumed to be: $x_{min} \le x \le x_{max}$; $y_{min} \le y \le y_{max}$; $z_{min} \le z \le z_{max}$. The coordinate of grid point $H(i,j,k)$ is (x_i,y_j,z_k)

$$\begin{cases} \Delta v = \Delta x \cdot \Delta y \cdot \Delta z \\ \Delta x = (x_{max} - x_{min})/m \\ \Delta y = (y_{max} - y_{min})/n \\ \Delta z = (z_{max} - z_{min})/k \end{cases} \tag{22}$$

$$\begin{cases} i = [(x - x_{min})/\Delta x] + 1 \\ j = [(y - y_{min})/\Delta y] + 1 \\ k = [(z - z_{min})/\Delta z] + 1 \end{cases} \tag{23}$$

$$\begin{cases} x_i = x_{min} + \Delta x \cdot (i - 1) \\ y_j = y_{min} + \Delta y \cdot (j - 1) \\ z_k = z_{min} + \Delta z \cdot (k - 1) \end{cases} \tag{24}$$

Here, x represents the radial distance of the droplets or particles in the cloud, y represents the height of the droplets or particles in the cloud, z represents the width distance of the droplets or particles in the cloud, and m_q represents the mass of particle $(q = 1, 2, ..., N)$ in the small rectangular box (ΔV).

https://dx.doi.org/10.1021/acsomega.0c05128
ACS Omega 2021, 6, 2085−2099

$$c_{ijk}^{(t)} = \frac{\sum_{q=1}^{N} m_q^{(t)}}{\Delta v} \tag{25}$$

Here, t represents the time and Δt represents the time step. Assuming that the small rectangular box ΔV is small enough, the concentration can be regarded as the concentration of the particle at that point. $c_{ijk}^{(t)}$ represents the condensed-phase concentration of the small rectangular box (i,j,k) at time t, which can be calculated using eq 25.

2.2.2. Dynamic System of Concentration Distribution. During the dispersal process, the particles or droplets move forward. The particles or droplets are modeled by single-particle motion dynamics, assuming that there is no collision between particles. The particle group resistance coefficient is added to supplement the interactions between the particles. Therefore, concentration distribution changes with the movement of particles at each moment. These changes include changes in the positions of particles or droplets and the gradual decline in the size of the particles or droplets due to stripping and evaporation effects.

The number of particles in each small rectangular box was different and varying with time because the particles are moving during cloud formation. Therefore, it is needed to calculate the concentration of particles of the small rectangular box at each moment. The concentration distribution of particles of the whole region can be obtained by combining the concentrations of all of the small rectangular boxes according to their distribution positions at that time.

$$A_k = \begin{bmatrix} a_{11k}, a_{12k}, \ldots, a_{1nk} \\ a_{21k}, a_{22k}, \ldots, a_{2nk} \\ a_{m1k}, a_{m2k}, \ldots a_{mnk} \end{bmatrix}$$

$$A_k = \overbrace{\underbrace{[0,0,\ldots,1,\ldots,0]^T}_{\text{The element of i th row is 1, the others is 0.}}}^{m} \times \overbrace{\underbrace{[0,0,\ldots,1,\ldots,0]}_{\text{The element of j th colum is 1, the others is 0.}}}^{n}$$

$$l = \overbrace{\underbrace{[0,0,\ldots,1,\ldots,0]^T}_{\text{The element of k th page is 1, the others is 0.}}}^{l}$$

$$\tilde{A} = A_1 : A_2 : \ldots : A_l \tag{27}$$

The transformation matrix $\tilde{A}$ is introduced, as in eq 24. It is defined that the element of the ith row, jth column, and kth page of the matrix with three dimensions is 1, and the other elements are all 0, which are shown in eq 24. a_{ijk} represents the element of the ith row, jth column, and kth page of the matrix with three dimensions. The 3D matrix $\tilde{A}$ $(m \times n \times l)$ can reflect the position distribution of each element in the matrix in Figure 4.

The transformation matrix $\tilde{A}$ is used to map the concentration value of a single cell calculated to the concentration matrix of the whole region and determine its position in the region. Therefore, the concentration distribution of the condensed phase is the superposition of the particle mass distribution of each small rectangular box obtained using eqs 26 and 29.

$$c_{ijk}^{(t)} = \frac{\sum_{q=1}^{N} m_q^{(t)}}{\Delta v} \times \tilde{A} \tag{28}$$

$$\tilde{c}_{ijk}^{(t)} = \frac{\sum_{q=1}^{N} m_q^{(t)}}{\Delta V} \times \tilde{A} \tag{29}$$

$$\tilde{C}^{(t)} = \sum \tilde{C}_{ijk}^{(t)} \tag{30}$$

where $c_{ijk}^{(t)}$ represents the condensed-phase concentration of the small rectangular box (i,j,k) at time t, $\tilde{c}_{ijk}^{(t)}$ represents the condensed-phase concentration matrix of the small rectangular box (i,j,k) at time t, and $\tilde{c}^{(t)}$ represents the condensed-phase concentration matrix of the whole region at time t.

The droplets decrease in size due to the evaporation effect and stripping effect during moving forward. The evaporation effect produces gas. In addition, aerodynamic friction exists on the droplet surface due to the velocity difference between the liquid and gas phases. Therefore, the little drops caused by the stripping effect are converted into the gas phase. Therefore, the mass of the gas generated at time $(t + \Delta t)$ can be obtained by the mass difference of the droplet at two moments (t and $t + \Delta t$) as eqs 31 and 32.

$$m_q'^{(t)} = m_q^{(t-\Delta t)} - m_q^{(t)} \tag{31}$$

$$c_{ijk}'^{(t)} = \frac{\sum_{q=1}^{N} [m_q^{(t-\Delta t)} - m_q^{(t)}]}{\Delta v}$$

$$c_{ijk}'^{(t)} = \frac{\sum_{q=1}^{N} m_q'^{(t)}}{\Delta v} \tag{32}$$

where $m_q'^{(t)}$ is the mass reduction of drops caused by evaporation, $c_{ijk}'^{(t)}$ represents the gas concentration of the small rectangular box (i,j,k) at time t, and $\tilde{c}'^{(t)}$ represents the gas concentration matrix of the small rectangular box (i,j,k) at time t, as shown in eq 33.

$$\tilde{c}_{ijk}'^{(t)} = \frac{\sum_{q=1}^{N} m_q'^{(t)}}{\Delta V} \times \tilde{A} \tag{33}$$

Suppose that the gas stays in its original position and does not move forward to simplify and speed up the calculation. The particle group keeps moving forward. When other particles move past this small rectangular box, the generated gas remains caused by the evaporation effect at the small rectangular boxes. Therefore, the gas concentration of these small rectangular boxes can be obtained by superposition of all of the mass of gas caused by every droplet passing through the small rectangular box as in eq 34.

$$\tilde{C}'^{(t)} = \sum \tilde{c}'^{(t)} \tag{34}$$

Since it is assumed that the generated gas stays in a stable state, it is needed to add up the gas produced at that moment with the gas produced before for the concentration distribution of the gas at each moment, as in eq 35.

$$\tilde{C}'^{(t)} = \tilde{C}'^{(t)} + \tilde{C}'^{(t-\Delta t)} \tag{35}$$

2.2.3. Correction Coefficient of Mass Conservation of Dynamic System. Particle dispersion is in a dynamic state.

https://dx.doi.org/10.1021/acsomega.0c05128
ACS Omega 2021, 6, 2085−2099

When the particles moving, they change, including size decrease due to the stripping effect caused by high speed and air resistance. The little drops caused by stripping effect are converted into gas phase caused by the aerodynamic friction existing on the droplet surface. In addition, the condensed phase is converted into a gas phase due to temperature differences.

According to the law of conservation of mass, droplet loss due to evaporation and stripping has the same mass as the formed gas. However, at the beginning of particle dispersal, the fuel expands to the point of rupture and produces a large number of particles. Tracking all of the particles can require considerable effort. Therefore, only a part of the fuel was selected based on the axisymmetric movement, with the particles in that part that were produced by fracture being tracked.

Moreover, to describe the particle dispersal concentration more accurately on the basis of the fact that the radius before the fuel ring expands to the point of fracture is the maximum initial particle size, the crushing function is introduced to refine the initial particle size. Therefore, to ensure that the total mass is always the same as the initial mass, the mass coefficient is introduced for correction to ensure the accuracy of the concentration distribution as in eq 36, where M is the initial total mass of the particle.

$$M^{(t)} = M_{\text{con}}^{(t)} + M_{\text{gas}}^{(t)} = k_i \cdot \left[\sum_{q=1}^{N} m_q^{(t)} + \sum_{q=1}^{N} m_q'^{(t)} \right] \tag{36}$$

$$k_i = M^{(t)} / \left(\sum_{q=1}^{N} m_q^{(t)} + \sum_{q=1}^{N} m_q'^{(t)} \right) \tag{37}$$

Here, m_i is the mass of the particle at time i and m_1 is the initial mass of the particle.

$$C_{\text{con}}(x, y) = k_i \cdot C^{(t)}$$
$$C_{\text{gas}}(x, y) = k_i \cdot C'^{(t)} \tag{38}$$

2.3. Fitting Formula and Correction of the Concentration Distribution Model. *2.3.1. Surface Fitting Formula and Correction Formula.* To better study the original model represented by discrete data, the first step is to convert the discrete data into continuous data. A smooth space surface $z = f(x, y)$ is fitted according to these data points. The inverse distance interpolation is applied for surface fitting since the data are known and discrete. The method of inverse distance interpolation was first proposed by Franke[26] and has been gradually developed in a variety of fields. The influence of each sample on the interpolation results decreases with the increase of distance. In the set of measured data (x_i, y_i, z_i) $(i = 1, 2, 3, ..., N)$, x_i, y_i, and c_i, respectively, represent the radial distance, height, and concentration of the droplets or particles, and N represents the number of droplets or particles. A smooth surface $Z = F(X, Y)$ is constructed to satisfy all of the data points. The point (x_i, y_i, z_i) is projected onto the XY plane, and the projection is $D(x_i, y_i)$ with the height of z_i. Then, the height z of any point $P(x, y)$ on the XY plane is affected by the height z_i of all points (x_i, y_i). The magnitude of the effect is related to the distances between this point and other points. The z_i of a point far away from P has less influence on P, while the point near P has more influence on P.

Therefore, the Z value of P point can be obtained by the weighted average of the influence of all points (x_i, y_i) on it. According to the basic premise of the distance weighted average method, the weight function must be the power of the reciprocal of distance.

2.3.2. Inverse Distance to a Power. Z_i is the value of $D(x_i, y_i)$, and $D(P, D_i)$ is the distance between $P(x, y)$ and $D(x_i, y_i)$, which can be abbreviated as d_i. To make the surface smooth and easy to calculate, here, the weight function takes the exponent 2. According to the above, the Z value of $P(x, y)$ can be obtained by eq 39.

$$F(x, y) = \begin{cases} \dfrac{\sum_{i=1}^{N} (d_i)^{-u} Z_i}{\sum_{i=1}^{N} (d_i)^{-u}} & D_i,\ d_i \neq 0 \\ Z_i & D_i,\ d_i = 0 \end{cases} \tag{39}$$

$$d_{ij} = [(x_i - x_j)^2 + (y_i - y_j)^2]^{1/2} \tag{40}$$

However, the above method is relatively simple and effective, but it suffers from a number of limitations: It is very computationally intensive to deal with a large number of data points. Only the distance from point $D(x_i, y_i)$ to point $P(x, y)$ is considered. However, the influence of direction is not considered. At each data point, there are no additional partial derivative constraints on the surface. In the field of D_i, due to $d_i \approx 0$, the calculation error is very sensitive. Therefore, Yao[27] proposed a number of improvements, e.g., ensuring the operation points are carefully selected; the direction weighting should be added to eliminate the influence of direction factors; the partial derivatives of each point should be reasonably estimated; and the neighborhood of D_i should be given to prevent overflow and reduce calculation errors.

(1) The inverse distance weighting method assumes that each measurement point has a local influence, which will decreases with the increase of distance.

The data points included in the calculation for eq 38 are reduced from all points to points near $P(x, y)$.

The contribution of data points outside the radius r is compensated by the data points within the radius. C' is the set of data points, and this ensures that the whole surface is continuously differentiable. For this reason, the weight function is defined as follows:

$$S(d) = \begin{cases} \dfrac{1}{d^2} & 0 < d \le \dfrac{r}{3^{1/2}} \\ \dfrac{27}{4r^2}\left[\left(\dfrac{d}{r}\right)^2 - 1\right]^2 & \dfrac{r}{3^{1/2}} < d \le r \\ 0 & d > r \end{cases}, r$$
$$= \max\{d_i\} \quad D_i \in C' \tag{41}$$

(2) The inverse distance weighting method only considers the distance from the measurement point $D(x, y)$ to $P(x, y)$ without considering the effect of its direction. For example, in the following two cases, we will get the same z value at $P(x, y)$. However, under reasonable circumstances, it is obvious that the Z value of point $P(x, y)$ in Figure 5a is closer to the Z value of point D_1 than that in Figure 5b. Conversely, the Z value of point $P(x, y)$ in

https://dx.doi.org/10.1021/acsomega.0c05128
ACS Omega 2021, 6, 2085−2099

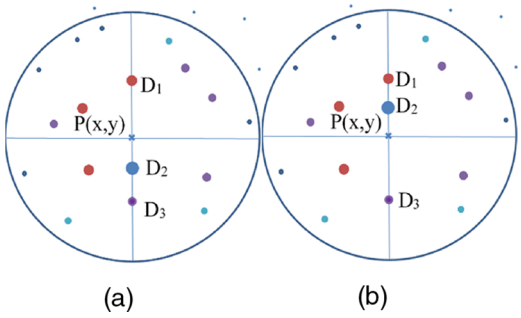

Figure 5. Schematic diagram of the influence of the value of the point $P(x, y)$ at the center of the circle on the value of is affected by the surrounding points. It is affected by the (a) direction of the value of $P(x, y)$ closer to the value of D_1 than D_3 and (b) direction of the value of $P(x, y)$ is closer to the value of D_3 than D_1.

Figure 5b should be closer to the Z value of point D_3 than that in Figure 5a.

In Figure 5, the size of the dots around the point $P(x, y)$ indicates the size of the weight. Points of the same color have the same weight. The weight is inversely proportional to the 2 power of the distance between the point and $P(x, y)$.

The influence of data points in different directions differs. As a result, the direction weighting can be measured by the projection of D_jP on D_iP. The cosine of the angle, $\cos(D_jPD_i)$, between $\overline{D_jP}$ and $\overline{D_iP}$ is introduced as a measure of distribution.

$$t_i = \frac{\sum_{D_i \in C'} S_i[1 - \cos(D_jPD_i)]}{\sum_{D_i \in C'} S_i} \tag{42}$$

The cosine of the angle here can be obtained by the dot product of the vectors.

$$\cos(D_jPD_i) = \frac{(x - x_i)(x - x_j) + (y - y_i)(y - y_j)}{d_i d_j} \tag{43}$$

Therefore, a new weight function is introduced when both distance and direction factors are considered.

$$W_i = (S_i)^2(1 + t_i) \tag{44}$$

(3) Here, the weighted average of the first-order difference quotient is taken as the approximation of the partial derivatives (A, B) in the x, y direction of $D_i(x, y)$.

$$\begin{cases} A_i = \dfrac{\sum_{D_j \in C''} W_i \frac{(z_j - z_i)(x_j - x_i)}{[d(D_jD_i)]^2}}{\sum_{D_j \in C''} W_i} \\ B_i = \dfrac{\sum_{D_j \in C''} W_i \frac{(z_j - z_i)(y_j - y_i)}{[d(D_jD_i)]^2}}{\sum_{D_j \in C''} W_i} \end{cases} \tag{46}$$

$$C'' = C'_{D_i} - D_i \tag{45}$$

For each point $D_i(x, y)$ belonging to C', it is necessary to calculate an increment ΔZ as the value of $P(x, y)$, which is added to the surface so that the surface has the desired partial derivative at the point $D_i(x, y)$.

$$\Delta Z_i = [A_i(x - x_i) + B_i(y - y_i)]\frac{v}{v + d_i} \tag{47}$$

A factor $\frac{v}{v + d_i}$ is introduced to control the influence of remote metering points on partial derivatives. As d_i changes from zero to infinity, the $\frac{v}{v + d_i}$ value monotonically changes from 1 to 0. When d_i is large, $\frac{v}{v + d_i}$ is approximately d_i^{-1}. However, the range of change in ΔZ may still be large. Therefore, the value of V can be adjusted to limit the range of change in ΔZ, which should not affect more than the value of Z. When V is set as follows

$$v = \frac{Q[\max\{Z_i\} - \min\{Z_i\}]}{[\max\{(A_i^2 + B_i^2)\}]^{1/2}} \tag{48}$$

no matter how d_i changes, it still exists:

$$|\Delta Z_i| \le Q[\max\{Z_i\} - \min\{Z_i\}] \tag{49}$$

The coefficient Q is arbitrary and can be changed for some surfaces. It is generally preferred: $0 < Q < 0.5$ Then, the partial derivative at $D_i(x, y)$ can be obtained as follows

$$\begin{cases} \dfrac{\partial}{\partial x}(\Delta Z_i)|_{\substack{x=x_i \\ y=y_i}} = A_i \\ \dfrac{\partial}{\partial y}(\Delta Z_i)|_{\substack{x=x_i \\ y=y_i}} = B_i \end{cases} \tag{50}$$

Therefore, the desired partial derivative of the surface is realized at the point $D_i(x, y)$.

(4) The rounding errors and truncation will cause significant errors when the point $P(x, y)$ is very close to a certain point $D_i(x, y)$. It will create difficulties in computer calculations, such as arithmetic overflow, etc. However, these problems can be avoided by establishing a neighborhood on $D_i(x, y)$. Once the point $P(x, y)$ falls into this neighborhood, we set $f(P) = Z$.

If $P(x, y)$ falls into several neighborhoods of $D_i(x, y)$ at the same time, their average Z value is taken as the Z of $P(x, y)$. The set composed of these $D_i(x, y)$ is defined as $N(P)$. Then, the concentration distribution surface function can be shown as follows

$$F(x, y) = \begin{cases} \dfrac{\sum_{D_i \in C'} W_i(Z_i + \Delta Z_i)}{\sum_{D_i \in C'} W_i}, & D_i,\ d_i > \xi \\ \dfrac{\sum_{D_i \in 'N(P)} Z_i}{\sum_{D_i \in 'N(P)} 1}, & D_i,\ d_i \le \xi \end{cases} \tag{51}$$

Here, W_i is the weight function, C' is the set of points participating in the operation, and C'' is the set of D_i in the epsilon neighborhood of $P(x, y)$ in C. Therefore, the law of concentration distribution of drops and particles during the dispersal of liquid and granular materials can be obtained by this model.

https://dx.doi.org/10.1021/acsomega.0c05128
ACS Omega 2021, 6, 2085−2099

3. RESULTS AND DISCUSSION

In this study, concentration distribution was predicted using a model for fuel dispersal, and the granular material and gas concentrations were calculated. In addition, the mean concentration was selected to validate the proposed model. An experiment was performed to support the proposed model, and the accuracy and reliability of the model were tested by comparing the experimental results to those obtained by the model.

3.1. Predictive Model for the Concentration Distribution of Fuel Dispersal. Simulation of liquid-phase fuel dispersal was performed, in which the model predicted fuel concentration distribution during dispersal. The conditions are presented in Table 1.

Table 1. Conditions of the Simulation

initial conditions of the simulation		
center charge	diameter	0.02 m
	height	0.4 m
	density	1.6×10^3 kg/m^3
	detonation pressure	1.5×10^{10} Pa
	initial multiple index of the detonation product	3.0
fuel	density	800 kg/m^3
	tensile strength	0.1 MPa
	viscosity coefficient	0.02 Pa s
shell	diameter	0.2 m
	height	0.4 m
	thickness	0.003 m
	density	7800 kg/m^3
	tensile strength	235 MPa
air	initial pressure	0.1 MPa
	sound velocity	340 m/s
	density	1.225 kg/m^3
	viscosity coefficient	1.8×10^{-5} Pa s

Figure 6 shows that the radius of the cloud increased quickly first. The radius of the cloud achieved a maximum value of 50 ms. In addition, the simulation shows that the maximum diameter of the cloud was 7.23 m and the initial velocity was about 537 m/s.

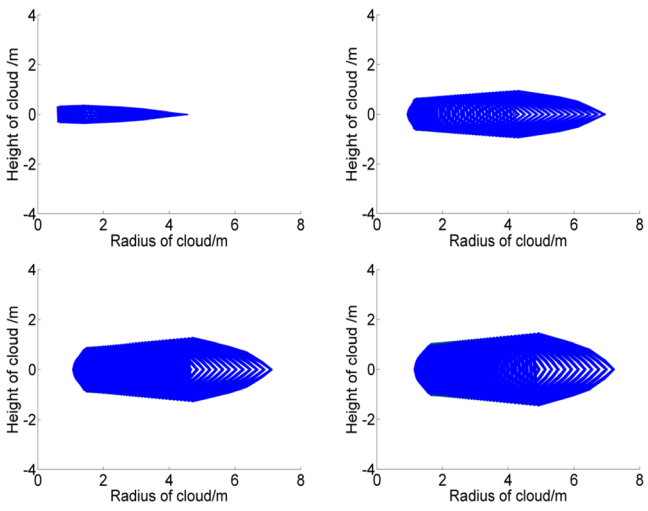

Figure 6. Process of particles cloud dispersal development for 10 kg of fuel at different times (t = 10, 50, 100, 200 ms).

Figure 7 shows the concentration of the liquid phase at the same horizontal level at different times, demonstrating that the concentration of liquid decreased with time during dispersal. Considering the central symmetry of the cylindrical cloud, a vertical section of the cylinder is extracted and studied as shown in Figure 9. The vertical section is taken as the bottom, and the cloud concentration is taken as the height to draw the concentration distribution on the vertical section. The mode is shown in Figure 8. Therefore, the condensed-phase cloud concentration of the vertical section is obtained. Figures 9−11 show that the drops/particles of the cloud edge have a higher concentration than the inner cloud at 200 ms. First, the concentration of the condensation phase was higher in the central region of the cloud. This is due to the detonation of the large number of particles produced. The concentration of the condensation phase began to decrease over time due to the breakdown of the drops/particles during flight. Furthermore, the particles kept moving forward. Meanwhile, a large amount of gasification occurred, which also caused the concentration of the liquid phase to decrease. During dispersal, some droplets slowed down or stopped moving due to resistance and some droplets continued to fly due to the effect of inertia until their velocity decreased to 0 m/s, and they stopped moving forward. Therefore, the concentration of the condensed phase gradually decreased and the high-concentration area gradually moved toward the edge of the cloud. The concentration of the liquid phase decreases with time until almost all of it is converted into gas phase, which indicates that the flammable liquid fuel is more effective in forming a gas cloud. The fuel dispersal device and parameter setting have a higher efficiency of fuel utilization.

Figure 12 shows the particle size distribution of longitudinal section highlighting that particle distribution occurred along the radial direction after dispersal at 200 ms. The initial maximum diameter of the particles or droplets is the critical thickness of the fuel before bursting. The initial velocity is the critical velocity before the fuel expands to rupture. The particles are mainly subjected to the action of air resistance and inertia force during the movement.

Therefore, the surface area of small particles is larger, the speed decreases quickly, and the distance of motion is short. Compared with the small particles, large particles have smaller surface area, slower speed reduction, larger inertia, and longer movement distance.

At the same time, the particles near the two ends of the cylindrical device have slower speed and shorter flight distance affected by the axial end effect. And the peel effect of the particles near the two ends is small because of the small difference with the air velocity. Therefore, the concentration near the two ends of the cylindrical device is larger. As a result, droplets with a small particle size were located inside the cloud, while droplets with a large particle size continued to move to the edge of the cloud along the axial direction as a result of higher inertia. Therefore, the particle concentration distributions in the upper and lower surfaces of cloud are relatively higher than in the center of cloud.

Figure 13 shows the gas concentration of the cloud at the same horizontal level at different points in time. It shows that the concentration of gas in the cloud center was larger than that at the cloud edge. Considering the central symmetry of the cylindrical cloud, a vertical section of the cylinder is divided.

https://dx.doi.org/10.1021/acsomega.0c05128
ACS Omega 2021, 6, 2085−2099

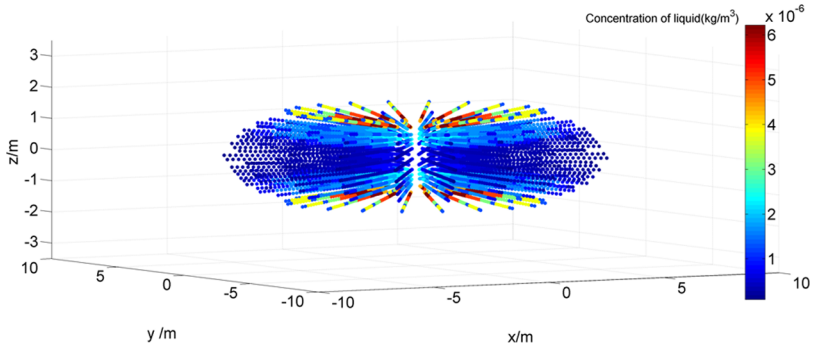

Figure 7. Liquid-phase concentration distribution longitudinal section formed by statics dispersal of liquid fuel at 200 ms.

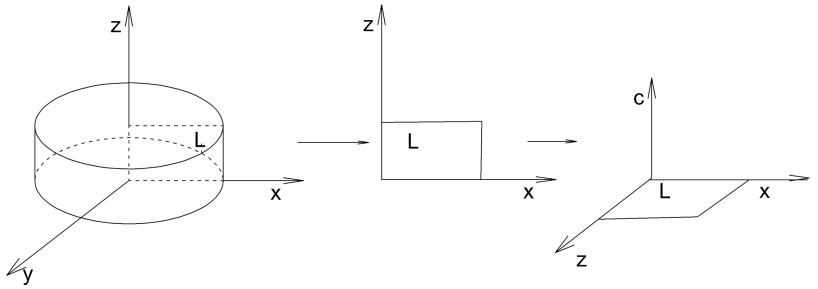

Figure 8. Vertical section L is cut from the cylindrical cloud along the radial direction; this rectangle L is taken as the base; and the cloud concentration C is set as height to plot the concentration distribution on the vertical section.

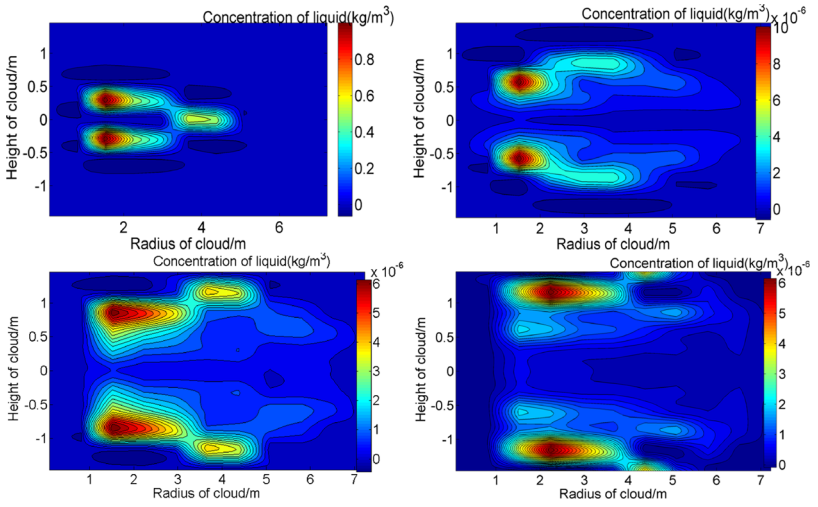

Figure 9. Liquid-phase concentration distribution longitudinal section formed by statics dispersal of liquid fuel (t = 10, 50, 100, 200 ms).

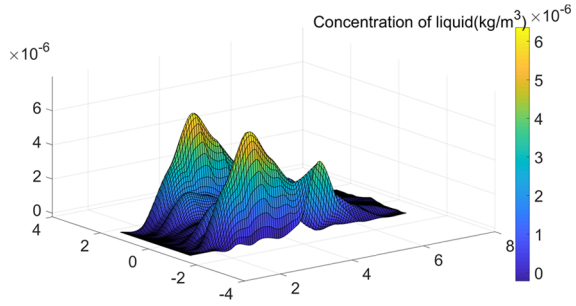

Figure 10. Liquid-phase concentration of cloud for 10 kg fuel dispersal at 200 ms.

The vertical section is taken as the base, and the cloud concentration is taken as the height. Therefore, the gas concentration of the vertical section is obtained as shown in Figures 14−16. First, the concentration of gas increased quickly. This is because a large concentration of liquid droplets was produced by fuel fragmentation. In addition to the liquid droplets, gas was produced by gasification. As time increased, the concentration of gas gradually stopped increasing due to the substantial reduction in the liquid drops. Therefore, the concentration of the gas phase was higher in the central zone and lower at the edge of the cloud.

Figures 11 and 16 show that the concentration of both gas and drop/particles in the center of the cloud is 0, corresponding to the central hollow zone. This corresponds with the hollowing of the center of the fuel cloud that was observed in the dispersal experiment.

https://dx.doi.org/10.1021/acsomega.0c05128
ACS Omega 2021, 6, 2085−2099

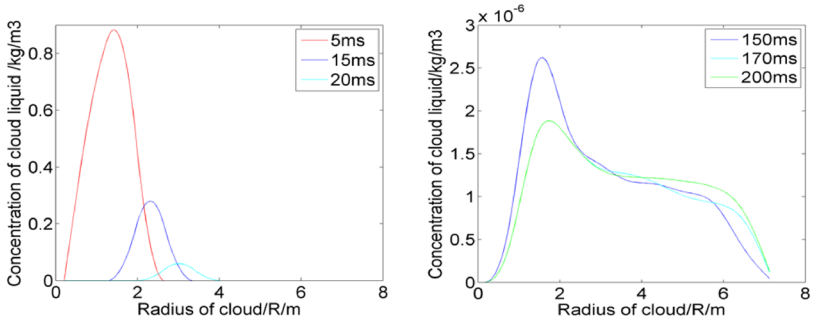

Figure 11. Liquid-phase concentration of 10 kg fuel dispersal at the same horizontal level along the radial direction (h = 0.02 m).

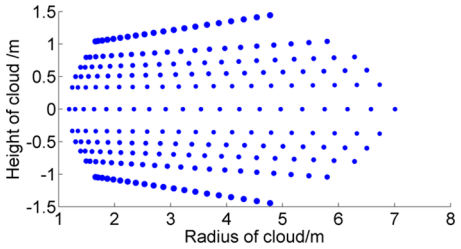

Figure 12. Droplet size distribution for 10 kg fuel dispersal of the longitudinal section of cloud at 200 ms (the particle size increases by 1×10^6 times).

There is a hollow area in the center of the cloud in which the fuel density is 0. The hollow center area tends to gradually move toward the edge of the cloud with time. This corresponds with the description of a hollow area in the theory of fuel dispersal. However, according to the different hollow areas that formed during the condensed phase and the gas phase, the hollow region of the cloud, where it seems no fuel appears, is not completely free of matter; instead, gas is evident at the edge of the hollow region.

3.2. Comparison with Experiments on Static Fuel Dispersal. An experiment on static fuel dispersion was conducted in the field to validate the proposed model. The dispersal device was a center tubular structure with a dimension of 200 mm × 400 mm. The shell was made of steel material with a thickness of 3 mm; the center charge was TNT with dimensions of 20 mm × 400 mm and a density of 1600 kg/m^3. The ratio of the center charge to fuel was about 2%. The total mass of dispersal fuel was 10 kg with a density of 800. Moreover, the photography frequency was 2000 frames/s, and the resolution ratio of each photo was 1280 × 800.

First, the variation of the cloud in the direction of the radius and height in each experiment was measured. Then, the cloud volume was calculated while assuming the cloud shape was a cylindrical geometric model and ignoring the central void. It was also assumed that the clouds were uniformly distributed. Finally, the average concentration of the clouds was calculated. The fuel dispersal process was recorded by high-speed photography and is shown in Figure 17.

In Figure 17, the shape of the fuel cloud was a flat cylinder. The size and volume of the cloud gradually increased with time, while the average concentration decreased. However, the development of the cloud rapidly increased first before increasing slowly. According to the dispersal experiment, as shown in Figure 17, and the simulation results, the cloud diffusion process can be divided into two stages. In the first stage, the fuel cloud disperses rapidly in a radial direction. In the second stage, the cloud stops expanding in the radial direction and the height of the cloud begins to increase.

The experimental results and the simulation results were then compared. The experimental data were selected when the cloud was basically stable. The characteristic parameters of the fuel cloud are shown in Table 2.

Comparing the experimental results with the simulation results shows that the cloud concentration distributions are consistent. The cloud development by the model (Figures 6, 9, and 14) was very similar to that observed in the explosive dispersal experiment (Figure 17). According to the experimental data, the cloud radius increased rapidly to a large value at 30 ms and then slowly increased. The cloud height increased the speed of dispersal after 30 ms. At 30 ms, the average cloud concentration was about 0.060 kg/m^3, and the cloud cover volume was 120 × 1.385 m^3. At 50 ms, the average cloud concentration was about 0.043 kg/m^3 and the cloud cover volume was 125 × 1.870 m^3. At 100 ms, the average cloud concentration was about 0.029 kg/m^3 and the cloud cover volume was 155 × 2.445 m^3. Coverage is a very important

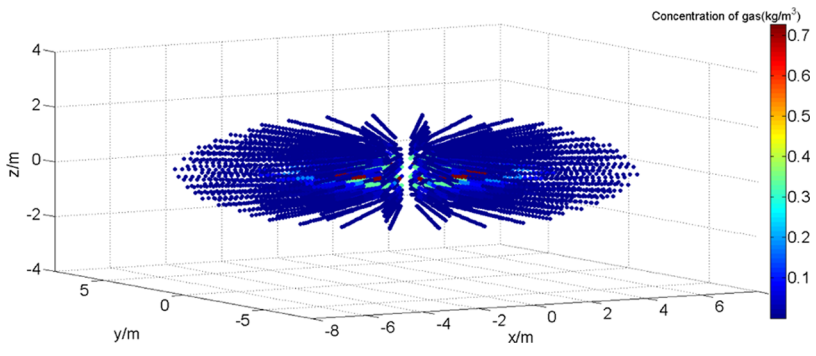

Figure 13. Gas-phase concentration of 10 kg fuel dispersal (200 ms).

https://dx.doi.org/10.1021/acsomega.0c05128
ACS Omega 2021, 6, 2085−2099

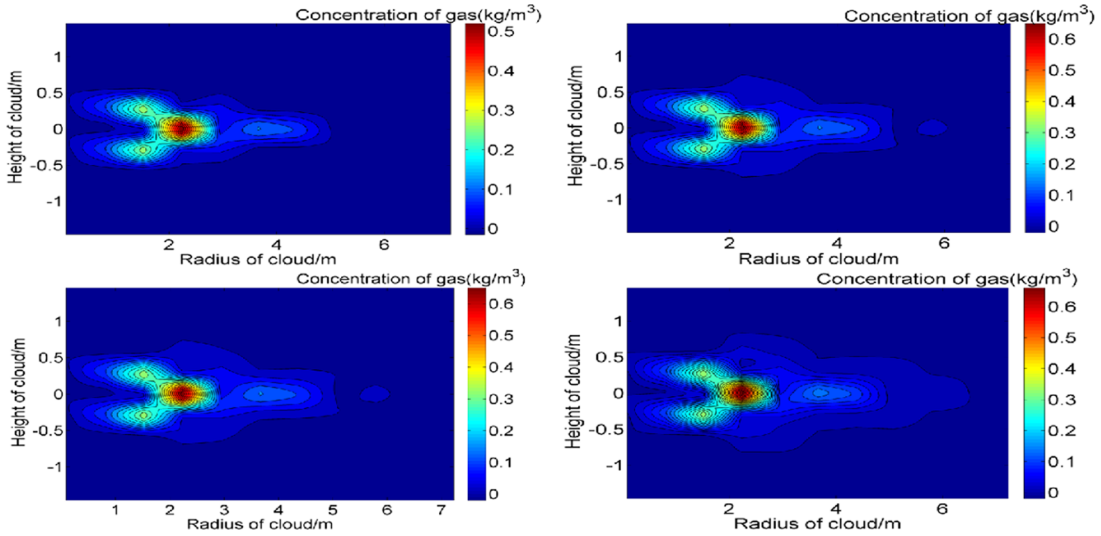

Figure 14. Gas-phase concentration distribution longitudinal section formed by statics dispersal of liquid fuel (t = 10, 50, 100, 200 ms).

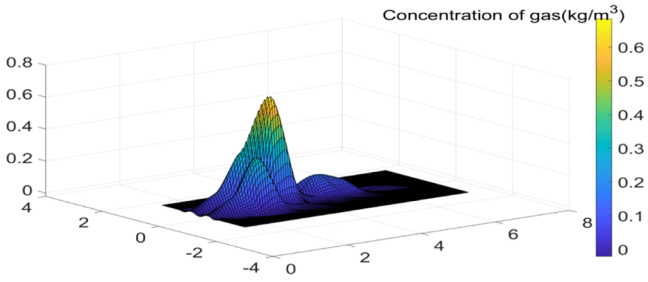

Figure 15. Gas-phase concentration of the vertical section L of cloud for 10 kg fuel dispersal at 200 ms.

indicator of dispersal. Therefore, the cloud concentration reached an optimum state at about 50 ms.

Combining the experimental results with the simulation results (Figures 6 and 11), several characteristics of the concentration distribution can be confirmed as follows:

Near the center of the cloud, the condensed-phase concentration increased rapidly before decreasing; the gas concentration increased first and then gradually stabilized. At the edge of the cloud, the concentration of the condensed phase first increased and then decreased to a certain value that tended to be stable. At this time, the concentration of the condensed phase in the center of the cloud was 0. Therefore, a hollow region appeared. The concentration of the condensed phase at the edge was higher, while the gas concentration was lower at the edge of the cloud.

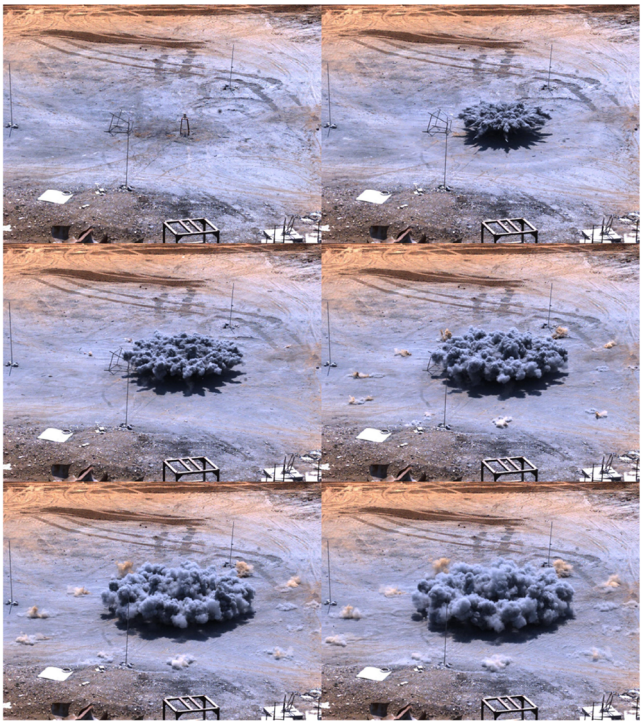

Figure 17. Cylindrical explosive dispersal of 10 kg fuel at different times (t = 0, 20, 30, 50, 100, 200 ms).

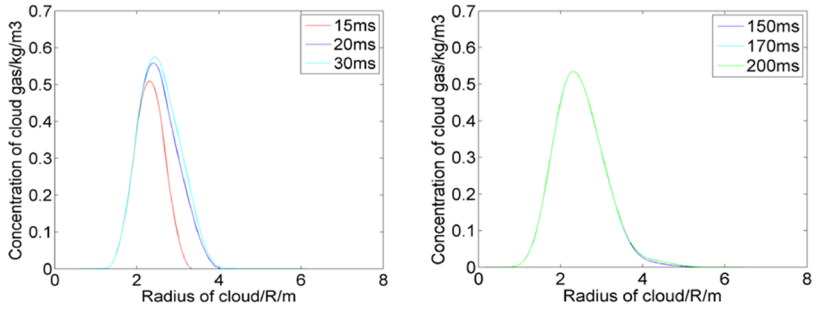

Figure 16. Gas-phase concentration of 10 kg fuel dispersal at the same horizontal level along the radial direction at different times (h = 0.02 m).

https://dx.doi.org/10.1021/acsomega.0c05128
ACS Omega 2021, 6, 2085−2099

Table 2. Comparisons of Experimental Results and Simulation Results

		time (ms)						
series code		10	20	30	50	100	150	200
experiment group	cloud radius (m)	3.971	5.310	6.171	6.311	7.024	7.125	7.337
	cloud height (m)	0.763	1.142	1.385	1.870	2.445	2.725	2.835
	average concentration (kg/m^3)	0.265	0.099	0.060	0.043	0.029	0.023	0.021
simulation group	cloud radius (m)	4.265	5.453	6.470	6.625	7.082	7.160	7.226
	cloud height (m)	0.717	1.068	1.408	1.848	2.394	2.702	2.819
	average concentration (kg/m^3)	0.244	0.100	0.055	0.039	0.027	0.023	0.022
error (%)	average concentration (kg/m^3)	−7.9	1.0	−8.3	−9.3	−6.89	0	4.7

At different positions in the radial direction of the cloud, the peak value of condensed-phase concentration decreased while increasing the distance from the center charge, that is, the condensed-phase peak concentration was found to be inversely proportional to the radial distance from the center charge. As the radial distance from the center charge decreased, the peak concentration occurred earlier, that is, the time of peak concentration of the condensed phase is proportional to the radial distance from the center charge.

After reaching peak concentration in a short period of time, the value of the gas concentration decreased as the distance from the center charge increased. In addition, the peak concentration of the cloud occurred at a position farther away from the center charge in a radial direction at a later point in time. As a result, the peak value of the gas concentration is proportional to the radial distance from the center charge, and the time of peak concentration is proportional to the radial distance from the center charge.

Combined with the results from the simulation and experiments, it can be well verified that cloud development can be divided into two stages. In the first stage, the cloud expands continuously in the radial direction and slowly in the axial direction. In the second stage, the cloud tends to be stable in the radial direction and the cloud begins to expand rapidly in the axial direction, which makes the cloud concentration more uniform. Finally, it tends to stabilize. In addition, characteristics such as drop/particle concentration distribution and gas concentration distribution can be calculated by applying the predictive model before conducting the experiments. These results can serve as a valuable reference for future research on liquid and granular material dispersal.

4. CONCLUSIONS

This study proposed a model for predicting the concentration distribution of explosive dispersal for liquid and granular material, which was validated using experimental data. The predictive model was based on the study of the concentration distribution of explosive dispersal in which there is no universal research method. This study provides a prediction tool to calculate in advance the gas concentration distribution and liquid concentration distribution at different locations and times. The variation in cloud concentration, including peak concentration, was studied based on the experimental and simulation results. The concentration of the gas phase was higher in the central zone, while the concentration of drops/particles was higher at the edge of the cloud. Moreover, the concentration of both gas and drop/particles in the center of the cloud was 0, which corresponds with the cloud hollowing observed in the dispersal experiment. Thus, the phenomenon of hollow fuel distribution was verified.

This model can enhance the accuracy and efficiency of secondary detonation of large-scale dispersal. Moreover, being able to predict the concentration distribution of dispersal can facilitate better risk management of fires and explosions.

The new concentration model can be used to grasp the overall development trend and law of fuel dispersion quickly before engineering analysis.

AUTHOR INFORMATION

Corresponding Author

Zhongqi Wang − *State Key Laboratory of Explosion Science and Technology, Beijing Institute of Technology, Beijing 100081, China;* orcid.org/0000-0003-2985-3333; Email: czqwang@bit.edu.cn

Authors

Xing Chen − *State Key Laboratory of Explosion Science and Technology, Beijing Institute of Technology, Beijing 100081, China; College of Environment and Chemical Engineering, Sichuan University of Science & Engineering, Zigong 643000, Sichuan, China*

En Yang − *State Key Laboratory of Explosion Science and Technology, Beijing Institute of Technology, Beijing 100081, China*

Jianping Li − *State Key Laboratory of Explosion Science and Technology, Beijing Institute of Technology, Beijing 100081, China*

Complete contact information is available at: https://pubs.acs.org/10.1021/acsomega.0c05128

Notes

The authors declare no competing financial interest.

ACKNOWLEDGMENTS

The authors thank the State Key Laboratory of Explosion Science and Technology in Beijing Institute of Technology and the College of Environment and Chemical Engineering of Sichuan University of Science & Engineering. This work was supported by the National Major Scientific and Technological Special Project during the 13th Five-year Plan Period, China (grant no.: 2016ZX05006-002), and the National Science Foundation of China (51678050).

REFERENCES

(1) Milne, A. M.; Parrish, C.; Worland, I. Dynamic fragmentation of blast mitigants. *Shock Waves* **2010**, *20*, 41−51.

(2) Milne, A. M.; Floyd, E.; Longbottom, A. W.; Taylor, P. Dynamic fragmentation of powders in spherical geometry. *Shock Waves* **2014**, *24*, 501−513.

(3) Grady, D. E. Local inertial effects in dynamic fragmentation. *J. Appl. Phys.* **1982**, *53*, 322.

https://dx.doi.org/10.1021/acsomega.0c05128
ACS Omega 2021, 6, 2085−2099

(4) Grady, D. *Fragmentation of Rings and Shells: The Legacy of N.F. Mott*; Springer-Verlag, 2010.
(5) Ripley, R. C.; Donahue, L.; Zhang, F. Jetting Instabilities of Particles from Explosive Dispersal. *J. Phys.: Conf. Ser.* **2012**, 1615−1618.
(6) Frost, D. L.; Ornthanalai, C.; Zarei, Z.; et al. Particle momentum effects from the detonation of heterogeneous explosives. *J. Appl. Phys.* **2007**, *101*, No. 113529.
(7) Zhang, F.; Ripley, R. C.; Yoshinaka, A.; Findlay, C. R.; Anderson, J.; von Rosen, B. Large-scale spray detonation and related particle jetting instability phenomenon. *Shock Waves* **2015**, *25*, 239−254.
(8) Allen, R. M.; Kirkpatrick, D. J.; Longbottom, A. W.; Milne, A. M.; Bourne, N. K. Experimental and numerical study of free-field blast mitigation. *AIP Conf. Proc.* **2004**, 823.
(9) Wang, Z.; Chen, H.; Liu, Y.; Guo, Y. Numerical simulation of the inert particles driven by explosives. *Acta Armamentarii* **2010**, 112−117.
(10) Grisaro, H.; Dancygier, A. N. Numerical study of velocity distribution of fragments caused by explosion of a cylindrical cased charge. *Int. J. Impact Eng.* **2015**, *86*, 1−12.
(11) Zhang, Q.; Bai, C.; Liu, Q.; Wang, Z. The near field dispersion of fuel air explosive under the action of uncoupled charge explosion. *J. Ballist.* **2000**, 26−29.
(12) Ding, J.; Weng, P.; Liu, J. Numerical study on liquid ring motion fragmentation in the initial phase of liquid explosive dispersal. *J. Hydrodyn. A* **2004**, *19*, 219−224.
(13) Ding, J.; Liu, J. A Numerical study of the whole process of liquid fuel explosion and cloud formation. *Chin. J. Expl. Propell.* **2001**, *24*, 20−23.
(14) Goroshin, S.; Frost, D. L.; Ripley, R. C.; Zhang, F. Measurement of particle density during explosive particle dispersal. *Propellants, Explos., Pyrotech.* **2016**, *41*, 245−253.
(15) Chen, X.; Wang, Z.; Liu, Y. A whole explosive dispersion process prediction model for fuel clouds. *Propellants, Explos., Pyrotech.* **2020**, *45*, 950−965.
(16) Liu, X. The Transient Multiphase Turbulent Cloud and Mist Concentration and Its Explosion Physical Characteristics Experiment. Beijing, Beijing Institute of Technology. Doctoral Dissertation, 2016, pp. 90−91.
(17) Yun, S.; Gao, F. In *Calculation of Explosive Instantaneous Detonation Parameters and Peak Pressure of Constant Detonation Wave*, Proceedings of the 11th Academic Exchange Meeting of the Committee of Physical Gas Dynamics of Chinese Aerodynamic Society, 2003; pp 173−177.
(18) Taylor, G. I.; Batchelor, G. K., Eds. *Scientific Papers, III: Aerodynamics and the Mechanics of Projectiles and Explosions*; Cambridge University Press, 1963.
(19) Zhang, S. Z. *Dynamics of Explosion and Impact*; Ordnance Industry Press, 1993; pp 138−140.
(20) Eidelman, S.; Burcat, A. Evolution of a detonation wave in a cloud of fuel droplets, I - Influence of igniting explosion. *AIAA J.* **1980**, *18*, 1103−1109.
(21) Engel, O. G. Fracmentation of water drops in the zone behind and air shock. *J. Res. Natl. Bur. Stand.* **1958**, *69*, 245.
(22) Schiller, L.; Naumann, Z. A Drag Coefficient Correlation. *Z. Ver. Dtsch. Ing.* **1935**, *77*, 318.
(23) Wen, C. Y.; Yu, Y. H. Mechanics of fluidization. *Chem. Eng. Prog., Symp. Ser.* **1966**, *62*, 100.
(24) Rhodes, M. J.; Wang, X. S.; Nguyen, M.; Stewart, P.; Liffman, K. Study of mixing in gas-fluidized beds using a DEM model. *Chem. Eng. Sci.* **2001**, *56*, 2859−2866.
(25) Feng, Y. Q.; Xu, B. H.; Zhang, S. J.; Yu, A. B.; Zulli, P. Discrete particle simulation of gas fluidization of particle mixtures. *AICHE J.* **2004**, *50*, 1713−1728.
(26) Franke, R. Scattered data interpolation: tests of some methods. *Math Comp.* **1982**, 181.
(27) Yao, R.; Cheng, F. A method of normalizing planedata points – weighted by distance. *J. Guilin Inst. Technol.* **1987**, 41−44.

https://dx.doi.org/10.1021/acsomega.0c05128
ACS Omega 2021, 6, 2085−2099